Measurements of Magnetic Field Fluctuations for Plasma Wave Investigation by the Search Coil Magnetometers (SCM) Onboard Bepicolombo Mio (Mercury Magnetospheric Orbiter)

Satoshi Yagitani, Mitsunori Ozaki, Fouad Sahraoui, Laurent Mirioni, Malik Mansour, Gérard Chanteur, Christophe Coillot, Sébastien Ruocco, Vincent Leray, Mitsuru Hikishima, et al.

Measurements of magnetic field fluctuations for Plasma Wave Investigation by the search coil magnetometers (SCM) onboard Bepicolombo Mio (Mercury Magnetospheric Orbiter)

Satoshi Yagitani[a], Mitsunori Ozaki[a], Fouad Sahraoui[b], Laurent Mirioni[b], Malik Mansour[b], Gerard Chanteur[b], Christophe Coillot[c], Sebastien Ruocco[d], Vincent Leray[e], Mitsuru Hikishima[f], Dominique Alison[b], Olivier Le Contel[b], Hirotsugu Kojima[g], Yoshiya Kasahara[a], Yasumasa Kasaba[h], Takashi Sasaki[i], Takahiro Yumoto[i], Yoshinari Takeuchi[i]

a Advanced Research Center for Space Science and Technology, Kanazawa University, Kakuma-machi, Kanazawa 920-1192, Japan

b Laboratoire de Physique des Plasmas, CNRS - Ecole Polytechnique - Sorbonne Université - Université Paris-Saclay - Observatoire de Paris-Meudon, Route de Saclay, 91128 Palaiseau, France

c Laboratoire Charles Coulomb (L2C) UMR5221, Université de Montpellier, CNRS, 34095 Montpellier, France

d LATMOS / CNRS - Université de Versailles -Sorbonne Université, 11, boulevard d'Alembert, 78280 Guyancourt, France

e NEXEYA C&F - Space technologies consulting, 5 Rue Boudeville - ZI de Thibaud, 31100 Toulouse, France

f Institute of Space and Astronautical Science, Japan Aerospace Exploration Agency, Kanagawa 252-5210, Japan

g Research Institute for Sustainable Humanosphere, Kyoto University, Uji, Kyoto 611-0011, Japan

h Planetary Plasma and Atmospheric Research Center, Graduate School of Science, Tohoku University, Sendai, Miyagi 980-8578, Japan

i NIPPI Corporation, 3175 Showa-machi, Kanazawa-ku, Yokohama 236-8560, Japan

Corresponding author:

Satoshi Yagitani

yagitani@is.t.kanazawa-u.ac.jp

Tel: +81-76-234-4858

Fax: +81-76-234-4859

Abstract

This paper describes the design and performance of the search coil magnetometers (SCM), which are part of the Plasma Wave Investigation (PWI) instrument onboard the BepiColombo/Mio spacecraft (Mercury Magnetospheric Orbiter), which will measure the electric field, plasma waves

and radio waves for the first time in Mercury's plasma environment. The SCM consists of two low-frequency orthogonal search coil sensors (LF-SC) measuring two components of the magnetic field (0.1 Hz – 20 kHz) in the spacecraft spin plane, and a dual-band search coil sensor (DB-SC) picking up the third component along the spin axis at both low-frequencies (LF: 0.1 Hz – 20 kHz) and high-frequencies (HF: 10 kHz – 640 kHz). The DB-SC and the two LF-SC sensors form a tri-axial configuration at the tip of a 4.6-m coilable mast (MAST-SC) extending from the spacecraft body, to minimize artificial magnetic field contamination emitted by the spacecraft electronics. After the successful launch of the spacecraft on 20 October 2018, an initial function check for the SCM was conducted. The nominal function and performance of the sensors and preamplifiers were confirmed, even with the MAST-SC being retracted and stowed in the spacecraft body, resulting in the detection of large interference signals likely from spacecraft electronics. The MAST-SC is scheduled for deployment after the Mercury orbit insertion of Mio in 2025, allowing the SCM to make the first higher frequency measurements of magnetic fluctuations in the Hermean magnetosphere and exosphere, and the local solar wind. These measurements will contribute to the investigation of fundamental problems in the Hermean plasma environment, including turbulence, magnetic reconnection, wave-particle interactions and particle acceleration.

Keywords

Search coil; Magnetic field fluctuation; Plasma wave; Radio wave; Mercury; Magnetosphere; Exosphere; Mercury Magnetospheric Orbiter (MMO); Mio; BepiColombo; solar wind; turbulence

1. Introduction

As part of the BepiColombo mission to Mercury (Hayakawa et al., 2004; Yamakawa et al., 2008; Benkhoff et al., 2010, this issue), the Plasma Wave Investigation (PWI) onboard the Mio spacecraft (Mercury Magnetospheric Orbiter: MMO) (Murakami et al., this issue) will measure the electric field, plasma waves, and radio waves for the first time in and around Mercury's magnetosphere and exosphere (Kasaba et al., 2010; this issue). Among the PWI subsystems, the search-coil magnetometers will measure the three components of the magnetic field fluctuations in the frequency range of 0.1 Hz to 20 kHz (which is defined as a "low frequency range" in the present paper) and one component in the range above 10 kHz up to 640 kHz (defined as a "high frequency range"). The data will allow us to carry out the first studies of low and high frequency electromagnetic waves and turbulence in different regions of the Hermean environment: bow shock, magnetosheath, magnetopause, magnetotail and solar wind. Moreover, they will make it possible to identify the processes of wave-particle interactions and energy dissipation when combined with the electric field and the plasma data from the PWI and MPPE suites (Kasaba et al., this issue, Karlsson et al., this issue; Saito et al., 2010).

The search coil magnetometers onboard Mio consist of low-frequency search coil sensors (LF-SC) detecting two orthogonal components of the magnetic field (0.1 Hz – 20 kHz) in the spacecraft spin plane, and a dual-band search coil sensor (DB-SC) picking up another component along the spin axis at both low-frequencies (LF: 0.1 Hz – 20 kHz) and high-frequencies (HF: 10 kHz – 640 kHz). The LF-SC and DB-SC sensors are installed on the tip of a long (4.6-m) coilable mast (MAST-SC) extending from the spacecraft body, to minimize magnetic field contamination emitted by the spacecraft electronics.

The search coil magnetometers will contribute to investigating various fundamental problems in the Hermean plasma environment such as turbulence, magnetic reconnection, wave-particle interactions and particle acceleration. Turbulence is a key process that allows transferring energy over the spatial scales of a nonlinear system, a phenomenon referred to as the turbulent cascade. Observations in the solar wind showed that this cascade can span a broad range of frequencies (or scales) that cover the MHD range (often referred to as the inertial range), where dissipation is thought to be negligible, down to the kinetic scales (sub-ion and electron ranges) where the processes of dissipation become important（Sahraoui et al., 2009). Similar observations have been made in the Hermean plasma environment, an example is shown in Figure 1 (Huang et al., 2020). One can observe three ranges of frequencies characterized by power-law scaling and are separated by spectral breaks that occur close to the gyrofrequency of protons and heavier ions (Na^+) (note that other characteristic scales/frequencies could not have been estimated because of the lack of the plasma data). The different power-law evidenced in the spectrum reflect the change in the nonlinear dynamics: the shallow spectrum at the lowest frequencies with a scaling close to f^{-1} recalls the so-

called “energy containing scales” in solar wind turbulence (e.g., Sahraoui et al., 2020). It is followed by the classical inertial range of MHD turbulence with a slope close to the Kolmogorov spectrum $f^{-5/3}$. The spectrum steepens further to $f^{-2.6}$ above the proton gyrofrequency, which indicates the transition to kinetic turbulence that has a scaling close to $f^{-2.8}$ as frequently reported in solar wind observations and numerical simulations (Sahraoui et al., 2010; Howes et al., 2011). Therefore, key questions arise as to which plasma modes (e.g., whistler, kinetic Alfvén wave (KAW)) dominate the cascade at the sub-ion scales and which processes are responsible for energy dissipation, thus converting it into thermal (heating) or suprathermal (acceleration) particles. The investigation of high frequency (small scale) turbulence is thus crucial to unravel the processes of turbulent energy dissipation and particle energization in space plasmas. Numerous studies have investigated plasma turbulence in planetary magnetospheres and the spatial evolution of its properties (e.g., magnetic energy spectra, intermittency, energy dissipation rate, from the shock to the inner magnetosphere of Jupiter (Tao et al., 2015), Saturn (Hadid et al., 2015), Mars (Ruhunusiri et al., 2017), Venus (Xiao et al., 2018) and, more recently, Mercury (Huang et al., 2020)). However, most of those studies were limited to large (MHD) scales because of the lack of high frequency measurements from the magnetic field that would have allowed one to investigate the small (electron) scales (Figure 1). This gap will be filled by the search-coil magnetometers onboard the Mio spacecraft (and by the other instruments of PWI), which will provide the first ever measurements in the Hermean environment of 3D magnetic field fluctuations in the frequency range between 0.1 Hz and 20kHz thanks to the LF-SC and DB-SC (LF) instruments, and in the range between 10 kHz and 640 kHz for the single component covered by the DB-SC (HF) instrument. Such measurements of higher frequencies are expected to allow studying plasma turbulence down to the electron scales which were not accessible to Messenger.

Another key process of particle energization in magnetized plasmas is magnetic reconnection. In turbulent plasmas, current sheets (and other coherent structures) form as a consequence of the nonlinear energy cascade from large to small scales. Thin current sheets were shown to form in numerical simulations and were observed in-situ by spacecraft. Their size can range from ion to electron scales (e.g., Perri et al., 2012). Measuring of such kinetic size current sheets and other coherent structures and associated wave activity will be made possible by the search-coil data from the LF-SC and DB-SC instruments. An example of measurement of intense whistler activity within electron scale structures by the MMS/SCM instrument is shown in Figure 2 (Huang et al., 2018).

Studies of magnetic reconnection can be completed by identifying the nature of the high frequency waves (e.g., whistler modes) that are responsible for the processes of wave-particle interactions near the reconnection sites (ion and electron diffusion regions), as generally done in reconnection studies in the Earth’s magnetosphere (e.g., Huang et al., 2012; Huang et al., 2017). Furthermore, fast plasma flows generated by reconnection or the kinetic ballooning-interchange

instability and which propagate through the Earth's magnetotail are also associated with a strong wave activity. Indeed, their propagation leads to the formation of sharp magnetic and density gradients (the so-called "dipolarization front") that can generate intense whistler and lower-hybrid waves (e. g. Breuillard et al., 2016; Sergeev et al., 2009). The latter, although being quasi-electrostatic waves, have a strong compressional magnetic component which, coupled with electric field measurements, allows one to estimate their phase speed (e.g., Le Contel et al., 2017). These fast flows can dissipate while propagating toward the planet due to intense emissions of KAW toward the auroral region (Chaston et al., 2012). Finally, electromagnetic and electrostatic solitary waves associated with electron phase space density holes that move along the background magnetic field were also detected in the vicinity of dipolarization fronts with 1-3 ms time scales (e. g. Matsumoto et al., 1994; Andersson et al., 2009; Le Contel et al., 2017). Dipolarization fronts were recently detected with a 10 s timescale in Mercury's magnetotail by MESSENGER (e.g. Sundberg, 2012) and were shown to be related to betatron and Fermi electron accelerations (e.g., Dewey 2017). However, high-frequency electromagnetic measurements were not available to investigate the wave-particle interactions. This gap will be filled by the Mio search coil magnetometers through the measurement of high frequency magnetic fluctuations. In particular, the DB-SC instrument can measure one component of the magnetic field fluctuations up to 640 kHz, which will allow covering all the local characteristic frequencies of the plasma (e.g., plasma frequency, electron cyclotron frequency). The high-frequency data from the DB-SC instrument will be also crucial to investigating the processes of radio wave emissions (e.g., solar type-II and type-III radio bursts) and mode conversion (from electrostatic to electromagnetic) predicted to occur near the plasma frequency f_{pe} and its harmonics (Bale et al., 1999; Cairns et al. 2003).

Another problem that can be investigated by the search-coil magnetometers of Mio is whistler-mode waves (e.g., chorus emissions), which were detected not only in the vicinity of Earth but also inside other planetary magnetospheres such as those of Jupiter, Saturn, and Uranus (Kurth and Gurnett, 1991), and were shown to play an important role in magnetized plasma dynamics through wave-particle interactions. Even in small crustal magnetic fields of Mars, whistler-mode chorus emissions were observed (Harada et al., 2016). In the complex magnetic fields around Mercury's magnetosphere, whistler-mode waves are expected to exist, and may be responsible for particle acceleration and precipitation down to Mercury's surface. The LF-SC and DB-SC data in combination with electric field data from the PWI instrument (Kasaba et al., this issue) will make it possible to measure wave polarizations, wave normal angles, Poynting vectors and phase velocities for identifying the generation and propagation mechanisms of different types of waves in the low-frequency range.

Finally, it is worth emphasizing that all these studies will be achieved across all the regions that will be explored by the BepiColombo/Mio mission (bow shock, magnetosheath, magnetopause,

magnetotail and nearby solar wind).

The BepiColombo/Mio spacecraft was successfully launched on 20 October 2018 and is now in cruise phase toward Mercury, integrated with the Mercury Planetary Orbiter (MPO) spacecraft (Benkhoff et al., this issue, Murakami et al., this issue). During the near-Earth commissioning phase (NECP) after the launch, an initial function check for the SCM was performed, where the nominal functions and performance of the sensors and preamplifiers were confirmed even under large magnetic interference from the spacecraft electronics due to the stowed configuration of the MAST-SC during cruise to Mercury. The search coil sensors will be deployed with the full extension of the MAST-SC after the insertion of the Mio spacecraft into orbit around Mercury in 2025.

To address the science targets described above, the search coil magnetometers onboard the Mio spacecraft have been carefully designed, built and calibrated to provide optimum performance even under a harsh thermal and radiation environment around Mercury. In this paper, the search coil magnetometer instruments onboard the Mio spacecraft are described in detail. Section 2 explains the hardware design of the LF-SC and DB-SC, followed by their electrical performance in Section 3. Section 4 provides the results of the initial function check during the NECP campaign, and Section 5 concludes the paper.

2. Hardware Design

2-1. Overall design

The search coil magnetometers (SCM) onboard Mio consist of two low-frequency search coil (LF-SC) sensors and one dual-band search coil (DB-SC) sensor, which form an orthogonal configuration allowing us to measure the full vector of the magnetic field fluctuations. Each of the two LF-SC sensors has a single solenoidal coil wound on a magnetic core, to detect the magnetic field in the low-frequency range between 0.1 Hz and 20 kHz. The DB-SC is composed of two pairs of solenoidal coils around a single magnetic core. Each pair is constituted of a primary winding connected via the preamplifier to a secondary winding ensuring the feedback flux needed to stabilize the response of the antenna (see also block diagram in Figure 5 and section 2.3). The two pairs are separated by a mutual reducer that allow picking up a low-frequency component (0.1 Hz to 20 kHz) and a high-frequency component (10 kHz to 640 kHz) separately (Coillot et al., 2010). The LF-SC and the DB-SC sensors and associated electronics system were designed and developed jointly by the Japanese and French teams, respectively, in close collaboration with each other. Both teams have built and provided the search coil magnetometers successfully flown on many spacecraft; e.g., Geotail, Cassini, Cluster, MMS, Themis, and Arase (for a comprehensive list of search coils onboard spacecraft, see Ozaki et al., 2018).

Figure 3 shows an illustration of the Mio spacecraft with electric field and magnetic field sensors. The SCM sensors are located on the tip of a 4.6-m mast (MAST-SC) extending from the

lower deck of the spacecraft, to minimize magnetic field interference from the instruments and their associated electronics on the spacecraft body. The two LF-SC sensors, B_α and B_β, are in the spacecraft spin plane, whereas the DB-SC sensor, B_γ, is parallel to the spin axis. In the spacecraft coordinate system marked as (X, Y, Z), two types of electric field sensors (32-m tip-to-tip long wire booms), WPT and MEFISTO, extend from the lower deck of the spacecraft along the X and Y axes in the spin plane, respectively, perpendicularly to the spin axis (+Z) (Karlsson et al., this issue). The MAST-SC, also deployed from the lower deck, makes an angle of –45 degrees from the +X direction in the spin plane. On the tip of the MAST-SC the two LF-SC sensors, B_α and B_β, are arranged to point into the (+X) and (–Y) directions, while the DB-SC sensor, B_γ, points into the –Z direction, respectively, in the spacecraft coordinate system.

The detailed configuration of the SCM sensors and the MAST-SC is illustrated in Figure 4. A set of tri-axial search coil sensors are placed on a top plate of an extendable mast, where the two orthogonal LF-SC sensors in the spin plane are arranged by 45 degrees from the mast axis, while the DB-SC sensor is perpendicular to them and directed along the spin axis. A 4.6-m coilable mast extends from a canister installed on the side panel of the lower deck. Though not shown in the figure, all the sensors on the top plate and the mast itself are covered with a thermal blanket to protect them from a thermally harsh environment around Mercury. The signal outputs from the sensors are connected through a wire harness to a preamplifier box (SC-Pre) mounted beside the mast canister, which are both placed inside the temperature-controlled spacecraft body. A temperature sensor is attached to the mast top plate, and a temperature sensor and a heater are installed in the preamplifier box. Also shown in Figure 4b are the flight models of the SC-Pre, the SCM sensors assembly (Figure 4c) and the MAST-SC in full extension during a ground test (Figure 4d).

Figure 5 shows a block diagram of the SCM sensors and preamplifiers. The low-frequency voltages picked up by the two LF-SC sensors, B_α and B_β, are fed to two preamplifiers (LF-SC-Pre) in the preamplifier box through a wire harness along the mast, and then transmitted to the two magnetic field channels, B_x and B_y, of the EWO-WFC/OFA receiver (EWO-WFC/OFA(B)) for waveform acquisition and their spectral analysis inside the PWI main electronics (PWI-E) (Kasaba et al., this issue). The signals from the low- and high-frequency sensors of DB-SC are conveyed to their respective preamplifiers (DB-SC-Pre) located also in the preamplifier box, where its low-frequency signals go to the B_z channel of the EWO-WFC/OFA(B) receiver together with the LF-SC signals, while its high-frequency signals are delivered to the magnetic field channel of the SORBET receiver in PWI-E (Moncuquet et al., 2006). In the EWO-WFC/OFA(B) receiver the three low-frequency magnetic field signals are first amplified (gain is 0 dB / 20 dB selectable) and band-limited below a cut-off frequency of 20 kHz through an analog front-end circuit with 7th-order elliptic low pass filters, and then digitally sampled at 65.536 kHz. A calibration signal is supplied by

the AM2P receiver in PWI-E to the low-frequency sensors, through the preamplifier box and the wire harness (Trotignon et al., 2006). Another calibration signal is supplied by SORBET to the high-frequency sensor of DB-SC. Feedback lines are connected from the preamplifier output to each of the DB-SC sensor coils in order to give the negative magnetic feedback. The calibration signals are applied to the sensors through their respective calibration coils. The overall power consumption of the sensors and preamplifiers is 384 mW for nominal operation. All the preamplifiers are housed in an aluminum box with thickness of at least 1 mm for protection against radiation.

Figure 6 presents the profiles of nominal sensitivities of the low-frequency and high-frequency sensors and preamplifiers, and their typical dynamic ranges when combined with the EWO and SORBET receivers. Also shown in the figure is a theoretical coverage in terms of spectral amplitude and frequency of plasma and radio waves known from the terrestrial environment and scaled to expected conditions in the Hermean magnetosphere and exosphere (Kasaba et al., this issue). For the low frequency range, the dynamic range of 78 dB in spectral amplitude is controlled in the EWO receiver by 0 dB and 20 dB gain steps. The high frequency signals have a dynamic range of 120 dB provided by the SORBET receiver. The targeted plasma waves should be almost entirely covered by the search coil's observable range. It is expected to cover as well the spin-modulated DC magnetic field B_0 at 0.25 Hz (two components in the spin plane).

Table 1 summarizes the flight model specifications of LF-SC and DB-SC.

2-2. Low-Frequency Search Coils (LF-SC)

The low-frequency search coils have two identical sensors, each of which picks up a single axial component of magnetic field. Figure 7a illustrates the structure of one axis sensor. The search coil sensor consists of a high-permeability magnetic core, two solenoid coils wound on it, and an electrostatic shield. The magnetic core is a 5 mm × 5 mm × 105 mm square bar composed of a number of 5 mm × 105 mm permalloy sheets of 0.1mm thickness, which are laminated with insulating adhesive to reduce the eddy current loss inside the core. The core is inserted into a plastic bobbin on which a primary solenoid coil with 16,000 turns is wound. Also wound on the same bobbin is a secondary coil of 20 turns used for applying a calibration signal to the sensor. The primary and secondary coils are made of a polyimide-coated copper wire of 0.1-mm diameter. To reduce the stray capacitance of the primary coil, the winding is divided into eight sections separated with flanges (Dalessandro et al, 2007). The coils and core are covered with an aluminum chassis that works as an electrostatic shield to reduce an electric field picked-up by the coil (Ozaki et al., 2015). To prevent the eddy current flowing on the surface of the shield which significantly reduces the magnetic flux inside the coil, a thin slit (gap) is put on each of the two opposite sides of the shield. The shield is supported by flanges of the bobbin with screws and a potting material. The bobbin is made of polyimide plastic, to withstand the harsh space environment. The picture of the

sensor (flight model) is shown in Figure 7b.

Figure 8 shows an equivalent circuit of the search coil sensor and preamplifier, which works as an LCR circuit with the inductance L_C, the resistance R_C, and the stray capacitance C_C due to the coil structure. The resistance R_{loss} includes the loss caused by the core, and C_{cable} is the capacitance of the harness cable (shielded and twisted wires) between the sensor output and the preamplifier. The sensor output signal is fed to a current-to-voltage (I-V converter) amplifier with a feedback resistance R_F (Ozaki et al., 2014). Due to the existence of the capacitance, the impedance of the sensor has a resonance frequency where the LC impedance goes to infinity, which is observed around a few kHz for the LF-SC sensors. The current source induced by the magnetic flux gathered by the core is picked up by the primary solenoid coil and is expressed as

$$I_C = \frac{V}{R_C + j\omega L_C}, V = j\omega\mu_{eff}NBS$$

where V is the induced voltage of the primary coil, B is the magnetic field to be measured, N is the number of turns of the primary coil, S is the cross section of the core, and ω is the angular frequency. The effective permeability μ_{eff} is given as a function of the core cross-section and length for a large value of core initial permeability (Seran and Fergeau, 2005); μ_{eff} = 159 for the permalloy core of 5 mm × 5 mm × 105 mm.

Two preamplifiers for the LF-SC sensors (LF-SC-Pre) are housed in the preamplifier box inside the spacecraft. Figure 9 shows a block diagram of the LF-SC sensors and preamplifiers. Here we adopted a preamplifier of current-to-voltage type (I-V converter) whose advantage is virtually to short out the stray and cable capacitances so that a flat gain response is obtained around the resonance frequency without any necessary feedback as in the conventional voltage amplifier. Similar current-to-voltage amplifiers have been used in the search coil magnetometers onboard the Arase satellite (Ozaki et al., 2018). The current-to-voltage amplifier is configured with a low-current-noise FET amplifier, to minimize the current noise. To achieve the largest possible dynamical range for the measurement, a second preamplifier for gain adjustment is put after the first current-to-voltage preamplifier.

Another buffer amplifier is used to receive and supply a calibration signal to the calibration coil of each sensor. The calibration signal is supplied from the AM2P receiver via the EWO board in PWI-E, which consists of a sequence of swept-frequency digital sine waves generated by a synthesizer (Kasaba et al., this issue; Trotignon et al., 2006). When received by the buffer amplifier, the calibration signal is smoothed by a low-pass filter that eliminates the discontinuity in the digital sine wave to create impulsive noises in the induced voltage on the primary coil due to the derivative nature of the Faraday's law of induction. The same calibration signal is distributed to the two LF-SC sensors, as well as to the low-frequency sensor of DB-SC, via the respective calibration coils.

The power supply (+12V) is filtered by an active low-pass filter to reduce high-frequency noise

and to improve the power supply rejection ratio (PSRR). The preamplifier circuit and its PCB layout were carefully designed to reduce the internal crosstalk between B_α and B_β components.

2-3. Dual-Band Search Coil (DB-SC)

The DB-SC sensors cover two distinct frequency bands: LF (0.1 Hz – 20 kHz) and HF (10 kHz – 640 kHz). The structure of DB-SC sensors is shown in Figure 10. On a single high-permeability magnetic core (ferrite core with high Curie temperature >200° C), the DB-SC sensor carries two separate sets of coils with a different number of windings to cover two different frequency ranges: a large number of turns (15,000) for low-frequencies and less turns (400) for high-frequencies. The two coils are separated by a mutual reducer which allows distinct measurements of the magnetic fluctuations in the two different frequency ranges (Coillot et al. 2010). The output voltages from these coils are applied to LF and HF preamplifiers (DB-SC-Pre).

The response of the instrument exhibits a resonance frequency that reduces its dynamic range. This problem is solved by injecting the preamplifier response into a feedback winding in order to flatten the transfer function. An advantage of this method is a transfer function that is insensitive to temperature variations on its flat part. Similarly to the LF-SC sensors, the calibration signals of the DB-SC (LF) will be delivered by the AM2P receiver via the EWO board whereas those of the DB-SC (HF) will be delivered by the SORBET receiver (pseudo-random-noise pulses). These calibration signals will be injected to the corresponding feedback windings. In-flight calibration achieves two goals, first to verify the optimal functioning of the instrument, and second to enable an estimate of the transfer functions and track any changes in time.

The electronics components used to achieve the low noise, low power consumption and wideband preamplifier have a long heritage since they have been used on previous missions such as Cassini (Gurnett et al., 2004), Cluster (Cornilleau-Wehrlin et al., 1997, 2003), THEMIS (Roux et al., 2008; Le Contel et al., 2008) and MMS (Le Contel et al., 2016). The preamplifiers were integrated into a 3D+ Technology. The components were plugged on a common PCB together with LF-SC-Pre in order to save mass and volume.

The main characteristics of this instrument are a broadband frequency measurement, with a physical length of 111 mm ~~length~~ (100 mm for the sensor and 11 mm for the extra length of the mechanical interface) and a mass of 65 g (which includes ~10 cm cable length), and a very low sensitivity: closer to the values of LF-SC in the frequency range from 1 Hz to 10 kHz for DB-SC (LF) (see Table 1) and below 30 fT/Hz$^{1/2}$ in the frequency range from 20 to 200 kHz for DB-SC (HF) and the possibility of in-flight calibration. The signals between the sensors and preamplifiers are transmitted by shielded and twisted wires. The LF and HF signals are to be fed to the EWO and SORBET receivers, respectively (Kasaba et al., this issue; Moncuquet et al., 2006).

346 **2-4. MAST-SC**

347 The tri-axial structure of the search coil sensors (SC assembly) is installed on the tip of MAST-
348 SC. Before extension, the mast structure shown in Figure 4 is wound into a compact coil shape and
349 stowed in a canister. Such a “coilable” mast structure has been successfully used onboard several
350 spacecraft (e.g., Geotail (Kokubun et al., 1994), Nozomi (Yamamoto and Matsuoka, 1998), Kaguya
351 (Tsunakawa et al., 2010) and Arase (Ozaki et al., 2018; Matsuoka et al., 2018)). It allows keeping
352 the sensitive (DC and AC) magnetometers away from the body of the spacecraft, and thus
353 minimizing interference from the spacecraft electronics. The advantages of the coilable mast
354 structure are its low mass and small volume in retracted configuration, and an accurate attitude of
355 tip-mounted sensors (within several degrees achievable) with a long length of extension (12 meters
356 for the case of Kaguya (Tsunakawa et al., 2010)). During the extension of the mast, the coil
357 structure is slowly unwound and released by an electric motor inside the canister, which lets the mast
358 extend outward due to a restorative force of each of the three longerons back to a straight wire. In a
359 fully extended configuration as illustrated in Figure 4, the three straight longerons in parallel are
360 supported by radial spacers. The harness wires between the sensors and preamplifiers are put along
361 the three longerons.

362 As is shown in Figure 4, the two LF-SC sensors and one DB-SC sensor are orthogonally
363 arranged by a supporting structure made of polyimide plastic. The whole tri-axial configuration of
364 the sensors is constructed on a circular top plate made of carbon fiber reinforced plastic (CFRP) that
365 has a large impedance so that no eddy current loss is expected there. Not shown in the figure, the
366 sensor assembly is covered with a thermal blanket box, whereas the whole mast is covered with a
367 thermal blanket called a "boot" to withstand the harsh thermal environment around Mercury. The
368 thermal blankets are made of multi-layered insulator (MLI).

369 The top plate is attached perpendicularly to the mast axis on which the pointing accuracy of the
370 sensors is kept within 6 degrees when the mast is fully extended, as measured by a ground test (see
371 Figure 4d). Though the inaccuracy of the sensor’s pointing direction could cause small uncertainties
372 (up to 6 degrees) in wave propagation analysis of the measurement, the misalignment could be
373 corrected by estimating the actual attitude of the sensors based on the spin modulation of the DC
374 magnetic field measured by the search coils around Mercury (see Section 5). The mass of the whole
375 MAST-SC structure is 4.36 kg, including search-coil sensors and thermal blankets. The temperature
376 on the top plate is monitored by a temperature sensor for house keeping. Even inside the thermal
377 blanket the expected temperatures at the top plate will range from -55° C during the cruise phase to
378 +200° C at Mercury’s orbit, over which the sensor will be turned on. All equipment including the
379 mast and sensor structures were designed to be tolerant in such a severely wide temperature range.
380 From the viewpoint of measurement by the search coil sensors, their transfer functions were
381 measured in the ground thermal test for a temperature range between -55° C to +200° C. A few dB

difference in the modulus and several degrees in the phase of the transfer functions in this temperature range were observed, compared with those shown in Figures 11 and 12 obtained at room temperature. By monitoring the temperature of the sensors as well as performing the onboard calibration, we will be able to compensate (calibrate) the temperature dependence to determine the actual transfer functions of the sensors during the cruise phase as well as around Mercury.

3. Electrical Characteristics

3-1. Low-Frequency Search Coils (LF-SC)

Figure 11 shows the frequency characteristics of gain, phase and sensitivity of the α-axis sensor of LF-SC measured on the ground before launch, which are similar to those for the β-axis sensor (not shown here). Figure 11a is the frequency characteristics of the gain, which is defined as the modulus of the transfer function from "the magnetic field picked up by the sensor" to "the voltage output by the preamplifier." An approximately flat gain is achieved between 500 Hz and 2 kHz (around a resonance frequency of a few kHz) by the current-to-voltage amplifier without the conventional feedback coil. The frequency characteristics of the phase of the transfer function is shown in Figure 11b. The sensitivity of the search coil is defined as a noise-equivalent magnetic induction (NEMI), which includes all the noise sources in the sensor and the preamplifiers. The NEMI is plotted in Figure 11c, which is almost compliant with the nominal sensitivity illustrated in Figure 6.

3-2. Dual-Band Search Coil (DB-SC)

Figure 12 presents the gain and phase profiles of DB-SC for the low-frequency sensor and the high-frequency sensor measured on the ground. The low-frequency profiles of the DB-SC gain and phase (Figures 12a and 12b) are similar, but not identical, to those of LF-SC. The high-frequency gain (Figure 12c) includes the gain of the SORBET receiver (see Moncuquet et al., 2006; Kasaba et al., this issue).

The resulting noise floor of the DB-SC sensors and preamplifiers is shown in Figure 13. Note that this noise floor (e.g., 5×10^{-5} nT/Hz$^{-1/2}$ at 1 kHz for DB-SC) is higher than that of the Cluster search-coil (e.g., 1.7×10^{-5} nT/Hz$^{-1/2}$ at 1 kHz for Cluster), because the latter has longer sensors (27 cm to be compared with the 10 cm of the LF-SC and DB-SC). However, the instrument will be sensitive enough to capture the magnetic field fluctuations in the Hermean environment, including the solar wind at 0.3 AU, which have higher amplitudes than those at 1AU (Sahraoui et al., 2011).

The low-frequency magnetic field signals from the LF-SC and DB-SC are fed to the EWO receiver, where the signals are band-limited through a 7th-order elliptic low-pass filter with a flat transfer function below a cut-off frequency of 20 kHz (Kasaba et al., this issue).

4. In-flight performance of the Search Coil Sensors: Near-Earth commissioning phase

After the successful launch of BepiColombo in October 2018, a Near-Earth Commissioning Phase (NECP) campaign was carried out in November, 2018, to confirm initially the nominal functioning of the onboard instruments. During the NECP campaign, most of the electronics parts of PWI were turned on and preliminary electric field and magnetic field data were acquired.

During the cruise phase the Mio spacecraft is positioned inside the sunshield (MOSIF) and integrated with the Mercury Planetary Orbiter (MPO) spacecraft (Milillo et al., 2010; this issue) and the Mercury Transfer Module (MTM) (Benkhoff, et al., this issue). Neither electric field sensors nor magnetic field sensors will be deployed until the separation of Mio from MPO after the Mercury orbit insertion scheduled in December 2025. Before the extension of MAST-SC, the search coil magnetometers will be kept outside the side panel of Mio on the retracted mast stowed in the canister. The SC sensors are thus expected to be subject to magnetic interference from the spacecraft electronics and its instruments.

For the low-frequency magnetic field measurement by the EWO receiver during the NECP campaign, only the dynamic spectral intensity of voltage, $|V| = \sqrt{V_x^2 + V_y^2 + V_z^2}$, was transmitted to the ground, where V_x, V_y and V_z are the voltage spectral intensities calculated onboard using the voltage waveforms measured in the B_x, B_y and B_z channels of the EWO-WFC/OFA(B) receiver. The voltage spectral intensities are obtained as $V_x = G_\alpha B_\alpha$, $V_y = G_\beta B_\beta$ and $V_z = G_\gamma B_\gamma$, where G_α, G_β and G_γ are the corresponding gains that include the sensors, the preamplifiers and the EWO electronics, and B_α, B_β and B_γ are the spectral intensities of magnetic field picked up by the LF-SC sensors (α and β) and the DB-SC (LF) sensor (γ). It is not possible to exactly convert the measured voltage spectra, $|V| = \sqrt{G_\alpha^2 B_\alpha^2 + G_\beta^2 B_\beta^2 + G_\gamma^2 B_\gamma^2}$, back into the magnetic field spectra, $|B| = \sqrt{B_\alpha^2 + B_\beta^2 + B_\gamma^2}$, since the gain profiles for the LF-SC (G_α, G_β) and for the DB-SC (LF) (G_γ) are not identical (see Figures 11 and 12). Here, we approximately calculated the magnetic field spectra using the "noise gain" calculated as $G_n \equiv |V_n|/|B_n|$, which is the noise voltage at the EWO output, $|V_n| = \sqrt{V_{nx}^2 + V_{ny}^2 + V_{nz}^2} = \sqrt{G_\alpha^2 B_{n\alpha}^2 + G_\beta^2 B_{n\beta}^2 + G_\gamma^2 B_{n\gamma}^2}$, divided by the noise-equivalent magnetic induction (NEMI) at the sensors, $|B_n| = \sqrt{B_{n\alpha}^2 + B_{n\beta}^2 + B_{n\gamma}^2}$, where (V_{nx}, V_{ny}, V_{nz}) and $(B_{n\alpha}, B_{n\beta}, B_{n\gamma})$ are the noise voltages expected to appear at the three channels of the EWO output and the three components of NEMI measured on the ground (see Figures 11 and 13), respectively. The noise gain should be accurately applied for evaluating the onboard noise levels (NEMI) of the sensors (see below).

Figure 14a shows the dynamic spectra of magnetic field $|B|$ during 01:00–02:00 UT on

November 10, 2018, measured in the frequency range between 64 Hz and 20 kHz. The monochromatic tones appearing around 200–300 Hz, 1.5 kHz, 4 kHz and 9 kHz, and the quasi-periodic wideband impulses below 10 kHz are, most likely, due to interference from some instruments onboard Mio, which remain to be identified.

Next, we evaluate the noise levels of the search coil magnetometers measured in space during the NECP campaign. Although contaminated with large magnetic interferences for most of the time as seen in Figure 14a, the observed spectra occasionally decreased down to the "quiet" values which might coincide with the noise-equivalent magnetic induction (NEMI) which represents the sensitivity of the search coil sensors. The frequency spectra of magnetic field calculated in such a way is plotted in Figure 14b, where the magnetic field spectrum averaged over the time period (one hour in Figure 14a) is shown with a red curve. In black is plotted the minimum value of magnetic field at each frequency bin observed during the same time period. These "quiet" values in the spectrum agreed well with the NEMI values $|B_n|$, especially in the frequency ranges of 700 Hz to 1.2 kHz and above 5 kHz. It is remarkable that, even not deployed, the NEMI measured in-flight agrees relatively well with the one measured on the ground.

It is worth recalling that the magnetic field intensities $|B|$ presented here were obtained from the combined (over the three components) voltage $|V|$ in a noisy environment as explained above. Further validation of the performance for each sensor separately will be achieved after the final insertion into Mercury orbit in 2025.

Figure 15 shows a result of the onboard calibration of the low-frequency sensors carried out on the same day. Supplying the swept-frequency calibration signals provided by AM2P through the EWO to the three low-frequency sensors via their respective calibration coils, we can obtain the transfer functions (i.e., calibration gains) of the sensors. The symbols represent the gain and phase of the transfer functions obtained onboard Mio, whereas the blue lines show the corresponding profiles measured during testing on the ground before launch. An excellent agreement was obtained between the onboard and ground profiles. One can note that the shape of the calibration gains in Figure 15 is a little bit different from those in Figures 11a and 12a, because the calibration gain includes effects of the calibration buffer amplifier with a low-pass filter as explained in Section 2.2.

These results validate and demonstrate the healthy functioning of the sensors and preamplifiers of LF-SC and DB-SC (LF), as well as the EWO and AM2P receivers onboard Mio.

Regarding the DB-SC (HF) sensor, several tests were performed, confirming the nominal functioning of the instruments with the SORBET receiver. An example is shown in Figure 16, which presents the SORBET spectrogram of DB-SC data obtained during NECP, where the transfer function of DB-SC has not been included yet. The spectrogram was computed over 4 successive frequency bands (see Figure 12c), each of which has a distinct automatic gain control (AGC) (AGC allows one to have a larger dynamical range of ~120dB (Moncuquet et al., 2006, Kasaba et al., this

issue)). Each frequency band has 32 logarithmically spaced channels, resulting in a total of 128 frequencies from 2.5 kHz to 620 kHz (central frequencies in the lowest and highest frequency bins of SORBET). As mentioned above, the LF-SC and DB-SC were not deployed during NECP. Therefore, most of the observed power in Figure 16 is likely to reflect interference from the spacecraft body and/or its instruments. This should be the case for the frequencies 90 kHz and 180 kHz where spikes are detected.

5. Summary

The SCM instrument onboard Mio consisting of LF-SC and DB-SC sensors and preamplifiers, was carefully designed and tested with the PWI, to detect the low-frequency magnetic vector field (0.1 Hz – 20 kHz) as well as the high-frequency magnetic field along the spacecraft spin axis (10 kHz – 640 kHz). In a series of commissioning tests conducted during the NECP campaign after launch, it was confirmed that the SCM worked well even on the retracted MAST-SC under a magnetically noisy environment due to the spacecraft electronics. After the Mercury orbit insertion in 2025, the MAST-SC will be fully deployed. The SCM will then make the first accurate measurements of magnetic fluctuations in Mercury's magnetosphere, exosphere, and in the nearby solar wind, and contribute to the understanding of plasma dynamics in those environments.

Once in orbit around Mercury, the Mio spacecraft will be spinning at the spin period of 4 sec. The spin motion will create a sinusoidal signal at 0.25 Hz of the DC magnetic field in the LF-SC sensors in the spin plane, whereas a much weaker modulation might be observed by the DB-SC sensor along the spin axis due to its possible misalignment with respect to the spin axis. Cross-calibration of SCM spin-modulated signals with simultaneous observations from the flux gate sensors (MGF) (Baumjohann et al., 2010; this issue) will improve estimates for the true attitude (pointing directions) of all search coil sensors. Furthermore, cross-calibration of the two sensors in their overlapping frequency range will allow to check the gain of each sensor.

The SCM will turn ON during the flybys at Earth, Venus and Mercury before the final insertion into orbit around Mercury in 2025, which gives us an opportunity to potentially measure the magnetic fluctuations in those environments. Even under a noisy environment on the retracted MAST-SC, we expect that the SCM will be able to pick up high amplitude plasma and radio waves during those flybys.

Acknowledgments

The authors would like to express their sincere thanks to all the Mio and BepiColombo project members, for the successful development, tests, launch and operations of the spacecraft. The SY and Japanese members would express their deep appreciation to Dr. Hiroshi Matsumoto, Dr. Isamu

Nagano, Mr. Yoshihiro Sato and Mr. Hiroshi Takano for their advice and support during the development of the LF-SC. The Japanese and French participation in the BepiColombo project are supported and funded by JAXA and CNES/CNRS, respectively.

References

L. Andersson, R. E. Ergun, J. B. Tao, A. Roux, O. Le Contel, V. Angelopoulos, J. W. Bonnell, J. P. McFadden, D. E. Larson, S. Eriksson, T. Johansson, C. M. Cully, D. N. Newman, M. V. Goldman, K.-H. Glassmeier, W. Baumjohann, New Features of Electron Phase Space Holes Observed by the THEMIS Mission. Phys. Rev. Lett. 102, 225004 (2009).

S. D. Bale, M. J. Reiner, J.-L. Bougeret, M. L. Kaiser, S. Krucker, D. E. Larson, and R. P. Lin. The source region of an interplanetary type II radio burst. Geophys. Res. Lett., 26:1573-1576 (1999).

W. Baumjohann, A. Matsuoka, W. Magnes, K.-H. Glassmeier, R. Nakamura, H. Biernat, M. Delva, K.Schwingenschuh, T. Zhang, H.-U. Auster, K.-H. Fornacon, I. Richter, A. Balogh, P. Cargill, C. Carr, M. Dougherty, T.S. Horbury, E.A. Lucek, F. Tohyama, T. Takahashi, M. Tanaka, T. Nagai, H. Tsunakawa, M. Matsushima, H. Kawano, A. Yoshikawa, H. Shibuya, T. Nakagawa, M.Hoshino, Y. Tanaka, R. Kataoka, B.J. Anderson, C.T. Russell, U. Motschmann, M. Shinohara. Magnetic field investigation of Mercury's magnetosphere and the inner heliosphere by MMO/MGF. Planet. Space Sci. 58, 1-2 (2010).

W. Baumjohann, A. Matsuoka, Y. Narita, W. Magnes, D. Heyner, K.-H. Glassmeier, R.Nakamura, D. Fischer, F. Plaschke, M. Volwerk, T. Zhang, H.-U. Auster, I. Richter, A. Balogh, C. Carr, M. Dougherty, T.S. Horbury, H. Tsunakawa, M. Matsushima, M. Shinohara, H. Shibuya, T. Nakagawa, M. Hoshino, Y. Tanaka, B.J. Anderson, C. T. Russell, U. Motschmann, F. Takahashi, A. Fujimoto. The BepiColombo-Mio Magnetometer en route to Mercury. Space Sci. Rev. this issue.

J. Benkhoff, J. van Casteren, H. Hayakawa, M. Fujimoto, H. Laakso, M. Novara, P. Ferri, H. Middleton, R. Ziethe. Bepicolombo—Comprehensive exploration of mercury: Mission overview and science goals. Planet. Space Sci. 58, 1-2 (2010).

J. Benkhoff, et al., Space Science Rev. this issue.

H. Breuillard, O. Le Contel, A. Retinò, A. Chasapis, T. Chust, L. Mirioni, D. B. Graham, F. D. Wilder, I. Cohen, A. Vaivads, Y. V. Khotyaintsev, P.-A. Lindqvist, G. T. Marklund, J. L. Burch, R. B. Torbert, R. E. Ergun, K. A. Goodrich, J. Macri, J. Needell, M. Chutter, D. Rau, I. Dors, C. T. Russell, W. Magnes, R. J. Strangeway, K. R. Bromund, F. Plaschke, D. Fischer, H. K. Leinweber, B. J. Anderson, G. Le, J. A. Slavin, E. L. Kepko, W. Baumjohann, B. Mauk, S.

A.Fuselier, R. Nakamura. Multispacecraft analysis of dipolarization fronts and associated whistler wave emissions using MMS data. Geophys. Res. Lett. 43, 14 (2016).

I. H. Cairns, S. A. Knock, P. A. Robinson, and Z. Kuncic. Type II Solar Radio Bursts: Theory and SpaceWeather Implications. Space Science Rev., 107:27-34 (2003).

C. C. Chaston, J. W. Bonnell, L. Clausen, V. Angelopoulos, Energy transport by kinetic-scale electromagnetic waves in fast plasma sheet flows. J. Geophys. Res. 117, A09202 (2012).

C. Coillot, J. Moutoussamy, R. Lebourgeois, S. Ruocco, G. Chanteur. Principle and performance of a dual-band search coil magnetometer: A new instrument to investigate fluctuating magnetic fields in space. IEEE Sensors J., 10, 2 (2010).

N. Cornilleau-Wehrlin et al., The Cluster Spatio-Temporal Analysis of Field Fluctuations (STAFF) Experiment. Space Sci. Rev. 79, 107 (1997).

N. Cornilleau-Wehrlin, G. Chanteur, S. Perraut, L. Rezeau, P. Robert, A. Roux, C. de Villedary, P. Canu, M. Maksimovic, Y. de Conchy, D. Hubert, C. Lacombe, F. Lefeuvre, M. Parrot, J. L. Pinçon, P. M. E. Décréau, C. C. Harvey, Ph. Louarn, O. Santolik, H. St. C. Alleyne, M. Roth, T. Chust, O. Le Contel, STAFF team. First results obtained by the Cluster STAFF experiment. Ann. Geophys., 21, (2003).

L. Dalessandro, F. da Silveira Cavalcante, J. W. Kolar., Self-capacitance of high-voltage transformers. IEEE Power Electron., 22, 5 (2007).

R. M. Dewey, J. A. Slavin, J. M. Raines, D. N. Baker, D. J. Lawrence, Energetic electron acceleration and injection during dipolarization events in Mercury's magnetotail. J. Geophys. Res. Space Physics. 122, 12 (2017).

D. A. Gurnett, W. S. Kurth, D. L. Kirchner, G. B. Hospodarsky, T. F. Averkamp, P. Zarka, A. Lecacheux, R. Manning, A. Roux, P. Canu, N. Cornilleau-Wehrlin, P. Galopeau, A. Meyer, R. Boström, G. Gustafsson, J. E. Wahlund, L. Åhlen, H. O. Rucker, H. P. Ladreiter, H. P. Ladreiter, W. Macher, L. J. C. Woolliscroft, H. Alleyne, M. L. Kaiser, M. D. Desch, W. M. Farrell, C. C. Harvey, P. Louarn, P. J. Kellogg, K. Goetz, and A. Pedersen, The Cassini radio and plasma wave investigation. Space Science Reviews, 114(1-4), 395-463. https://doi.org/10.1007/s11214-004-1434-0 (2004).

L. Z. Hadid, F. Sahraoui, K. H. Kiyani, A. Retinò, R. Modolo, P. Canu, A. Masters, M. K. Dougherty, Nature of The MHD and Kinetic Scale Turbulence in the Magnetosheath of Saturn: Cassini Observations. Astrophys. J. Lett. 813, 2 (2015).

Y. Harada, L. Andersson, C. M. Fowler, D. L. Mitchell, J. S. Halekas, C. Mazelle, J. Espley, G. A. DiBraccio, J. P. McFadden, D. A. Brain, S. Xu, S. Ruhunusiri, D. E. Larson, R. J. Lillis, T. Hara, R. Livi, B. M. Jakosky, MAVEN observations of electron- induced whistler mode waves in the Martian magnetosphere. J. Geophys. Res. Space Physics. 121, 10 (2016).

H. Hayakawa, Y. Kasaba, H. Yamakawa, H. Ogawa, T. Mukai, The Bepicolombo/MMO model payload and operation plan. Adv. Space Res. 33, 12 (2004).

G. G. Howes, J. M. TenBarge, W. Dorland, E. Quataert, A. A. Schekochihin, R. Numata, and T. Tatsuno, Gyrokinetic Simulations of Solar Wind Turbulence from Ion to Electron Scales, Phys. Rev. Lett., 107, 035004 (2011).

S. Y. Huang et al., Observations of turbulence within reconnection jet in the presence of guide field. Geophys. Res. Lett. 39, L11104 (2012).

S. Y. Huang et al., Occurrence rate of whistler waves in the magnetotail reconnection region. J. Geophys. Res. Space Physics. 122, 7 (2017).

S. Y. Huang, F. Sahraoui, Z.G. Yuan, O. Le Contel, H. Breuillard, J.S. He, J.S. Zhao, H.S. Fu, M. Zhou, X.H. Deng, X.Y. Wang, J.W. Du, X.D. Yu, D.D. Wang, C.J. Pollock, R.B. Torbert, J.L. Burch, Observations of whistler waves correlated with electron-scale coherent structures in the magnetosheath turbulent plasmas, The Astrophysical Journal, 861:29 (2018)

S. Y. Huang, Q. Y. Wang, F. Sahraoui, Z. G. Yuan, Y. J. Liu, X. H. Deng, W. J. Sun, K. Jiang, S. B. Xu, X. D. Yu, Y. Y. Wei, and J. Zhang, Analysis of Turbulence Properties in the Mercury Plasma Environment Using MESSENGER Observations, The Astrophysical Journal, 891:159 (6pp) (2020).

T. Karlsson, Y. Kasaba, J.-E. Wahlund, P. Henri, L. Bylander, W. Puccio, K. Ishisaka, S.-E. Jansson, H. Kojima, A. Kumamoto, L. Ahlen, A. Eriksson, M. Morooka, The MEFISTO and WPT electric field sensors of the Plasma Wave Investigation on the BepiColombo Mio (Mercury Magnetospheric Orbiter). Space Sci. Rev. this issue.

Y. Kasaba, J.-L. Bougeret, L.G. Blomberg, H. Kojima, S. Yagitani, M. Moncuquet, J.-G. Trotignon, G. Chanteur, A. Kumamoto, Y. Kasahara, J. Lichtenberger, Y. Omura, K. Ishisaka, H. Matsumoto, The Plasma Wave Investigation (PWI) onboard the BepiColombo/MMO: First measurement of electric fields, electromagnetic waves, and radio waves around Mercury. Planet. Space Sci. 58, 1–2 (2010). doi:10.1016/j.pss.2008.07.017

Y. Kasaba, H. Kojima, M. Moncuquet, J. E. Wahlund, S. Yagitani, F. Sahraoui, P. Henri, T. Karlsson, Y. Kasahara, A. Kumamoto, K. Ishisaka, K. Issautier, G. Wattieaux, T. Imachi, S. Matsuda, J. Lichtenberger, H. Usui, Plasma wave investigation (PWI) aboard Mio / Bepicolombo Mercury Magnetospheric Orbiter (MMO) on the trip to the first measurement of electric fields, electromagnetic waves, and radio waves around Mercury. Space Sci. Rev. this issue (2020). doi:10.1007/s11214-020-00692-9

S. Kokubun, T. Yamamoto, M. H. Acuna, K. Hayashi, K. Shiokawa, H. Kawano, The GEOTAIL magnetic field experiment. J. Geomag. Geoelectr. 46, (1994).

W. S. Kurth, D. A. Gurnett, Plasma waves in planetary magnetospheres. J. Geophys. Res. 96, S01 (1991).

O. Le Contel, A. Roux, P. Robert, C. Coillot, A. Bouabdellah, B. de la Porte, D. Alison, S. Ruocco,V. Angelopoulos, K. Bromund, C. C. Chaston, C. Cully, H. U. Auster, K. H. Glassmeier, W. Baumjohann, C. W. Carlson, J. P. McFadden, D. Larson, First results of the THEMIS Search Coil Magnetometers. Space Sci. Rev. 141, (2008).

O. Le Contel, P. Leroy, A. Roux, C. Coillot, D. Alison, A. Bouabdellah, L. Mirioni, L. Meslier, A. Galic, M. C. Vassal, R. B. Torbert, J. Needell, D. Rau, I. Dors, R. E. Ergun, J. Westfall, D. Summers, J. Wallace, W. Magnes, A. Valavanoglou, G. Olsson, M. Chutter, J. Macri, S. Myers, S. Turco, J. Nolin, D. Bodet, K. Rowe, M. Tanguy, B. De la Porte, The Search-Coil Magnetometer for MMS. Space Sci. Rev. 199, 1-4 (2016).

O. Le Contel, R. Nakamura, H. Breuillard, M. R. Argall, D. B. Graham, D. Fischer, A. Retinò, M. Berthomier, R. Pottelette, L. Mirioni, T. Chust, F. D. Wilder, D. J. Gershman, A. Varsani, P.-A. Lindqvist, Y. V. Khotyaintsev, C. Norgren, R. E. Ergun, K. A. Goodrich, J. L. Burch, R. Torbert B., J. Needell, M. Chutter, D. Rau, I. Dors, C. T. Russell, W. Magnes, R. J. Strangeway, K. R. Bromund, H. Y. Wei, F. Plaschke, B. J. Anderson, G. Le, T. E. Moore, B. L. Giles, W. R. Paterson, C. J. Pollock, J. C. Dorelli, L. A. Avanov, Y. Saito, B. Lavraud, S. A. Fuselier, B. H. Mauk, I. J. Cohen, D. L. Turner, J. F. Fennell, T. Leonard, A. N. Jaynes, Lower Hybrid Drift Waves and Electromagnetic Electron Space-Phase Holes Associated With Dipolarization Fronts and Field-Aligned Currents Observed by the Magnetospheric Multiscale Mission During a Substorm, J. Geophys. Res. Space Physics. 122, 12 (2017).

H. Matsumoto, H. Kojima, T. Miyatake, Y. Omura, M. Okada, I. Nagano, M. Tsutsui, Electrotastic solitary waves (ESW) in the magnetotail: BEN wave forms observed by Geotail. Geophys. Res. Lett. 21, (1994).

A. Matsuoka et al., The ARASE (ERG) magnetic field investigation. Earth Planets Space. 70, 43 (2018).

A. Milillo, M. Fujimoto, E. Kallio, S. Kameda, F. Leblanc, Y. Narita, G. Cremonese, H. Laakso, M. Laurenza, S. Massetti, S. McKenna-Lawlor, A. Mura, R. Nakamura, Y. Omura, D. Rothery, K. Seki, M. Storini, P. Wurz, W. Baumjohann, E. Bunce, Y. Kasaba, J. Helbert, A. Sprague, Hermean environment wg members, The bepicolombo mission: An outstanding tool for investigating the hermean environment, planet. Planet. Space Sci. 58, 1-2 (2010).

A. Milillo, M. Fujimoto, G. Murakami, J. Benkhoff, J. Zender, S. Aizawa, M. Dosa, L. Griton, D. Heyner, G. Ho, S. Imber, X. Jia, T. Karlsson, R.M. Killen, M. Laurenza, S. Lindsay, S. McKenna-Lawlor, A. Mura, J. Raines, D. Rothery, N. André, W. Baumjohann, A. Berezhnoy, P. Bourdin, E. Bunce, F. Califano, J. Deca, S. de la Fuente, C. Dong, C. Grava, S. Fatemi, P. Henri, S. Ivanovski, B. V. Jackson, M. James, E. Kallio, Y. Kasaba, E. Kilpua, M. Kobayashi, B. Langlais, F. Leblanc, C. Lhotka, V. Mangano, A. Martindale, S. Massetti, A. Masters, M. Morooka, Y. Narita, J.S. Oliveira, D. Odstrcil, S. Orsini, C. Plainaki, F. Plaschke, F. Sahraoui,

K. Seki, J. Slavin, R. Vainio, P. Wurz, S. Barabash, C. Carr, D. Delcourt, K.-H. Glassmeier, M. Grande, M. Hirahara, J. Huovelin, O. Korablev, H. Kojima, H. Lichtenegger, S. Livi, A. Matsuoka, R. Moissl, M. Moncuquet, K. Muinonen, E. Quemerais, Y. Saito, S. Yagitani, I. Yoshikawa, J.-E. Wahlund, Investigating Mercury's environment with the two-spacecraft BepiColombo mission. Space Science Rev., this issue.

M. Moncuquet, H. Matsumoto, J-L. Bougeret, L. G. Blomberg, K. Issautier, Y. Kasaba, H. Kojima, M. Maksimovic, N. Meyer-Vernet, P. Zarka, The radio waves and thermal electrostatic noise spectroscopy (SORBET) experiment on BEPICOLOMBO/MMO/PWI: Scientific objectives and performance. Adv. Space Res. 38, 4 (2006).

G. Murakami, H. Hayakawa, H. Ogawa, S. Matsuda, T Seki, Y. Kasaba, Y. Saito, I. Yoshikawa, M. Kobayashi, W. Baumjohann, A. Matsuoka, H. Kojima, S. Yagitani, M. Moncuquet, J.-E. Wahlund, D. Delcourt, M. Hirahara, S. Barabash, O. Korablev, M. Fujimoto, Mio ─ First comprehensive exploration of Mercury's space environment: mission overview. Space Sci. Rev. this issue.

M. Ozaki, S. Yagitani, H. Kojima, K. Takahashi, A. Kitagawa, Current-sensitive CMOS preamplifier for investigating space plasma waves by magnetic search coils. IEEE Sensors J. 14, 2 (2014).

M. Ozaki, S. Yagitani, K. Takahashi, T. Imachi, H. Koji, R. Higashi, Equivalent circuit model for the electric field sensitivity of a magnetic search coil of space plasma. IEEE Sensors J. 15, 3 (2015).

M. Ozaki, S. Yagitani, Y. Kasahara et al. Magnetic Search Coil (MSC) of Plasma Wave Experiment (PWE) aboard the Arase (ERG) satellite. Earth Planets Space. 70, 76 (2018).

S. Perri, M. L. Goldstein, J. C. Dorelli, F. Sahraoui, Detection of Small-Scale Structures in the Dissipation Regime of Solar-Wind Turbulence. Phys. Rev. Lett. 109, 191101 (2012).

A. Roux, O. Le Contel, P. Robert, C. Coillot, A. Bouabdellah, B.d. la Porte, D. Alison, S. Ruocco, M.C. Vassal, The search coil magnetometer for THEMIS. Space Sci. Rev. 141, 1-4 (2008).

S. Ruhunusiri et al., Characterization of turbulence in the Mars plasma environment with MAVEN observations. J. Geophys. Res. Space Physics, 122, 1 (2017).

F. Sahraoui, M. L. Goldstein, P. Robert, Yu. V. Khotyaintsev, Evidence of a Cascade and Dissipation of Solar-Wind Turbulence at the Electron Gyroscale. Phys. Rev. Lett., 102, 231102 2009.

F. Sahraoui, M. L. Goldstein, G. Belmont, P. Canu & L. Rezeau, Three dimensional k-spectra of turbulence at sub-proton scales in the solar wind, Phys. Rev. Lett., 105, 131101 (2010)

F. Sahraoui et al., Multi-spacecraft investigation of space turbulence: Lessons from Cluster and input to the Cross-Scale mission. Planet. Space Sci. 59, 7 (2011).

F. Sahraoui, L. Z. Hadid, S. Y. Huang, Magnetohydrodynamic and kinetic scale turbulence in the near-Earth space plasmas: a (short) biased review, Reviews of Modern Plasma Physics, 4:4, https://doi.org/10.1007/s41614-020-0040-2 (2020)

Y. Saito, J.A. Sauvaud, M. Hirahara, S. Barabash, D. Delcourt, T. Takashima, K. Asamura, Scientific objectives and instrumentation of Mercury Plasma Particle Experiment (MPPE) onboard MMO. Planet. Space Sci. 58, 1–2 (2010).

H. C. Séran, P. Fergeau, An optimized low-frequency three-axis search coil magnetometer for space research. Rev. Sci. Instrum. 76, 044502 (2005).

V. Sergeev, V. Angelopoulos, S. Apatenkov, J. Bonnell, R. Ergun, R. Nakamura, J. McFadden, D. Larson, A. Runov, Kinetic structure of the sharp injection/dipolarization front in the flow-braking region. Geophys. Res. Lett. 36, L21105 (2009).

T. Sundberg, et al., MESSENGER observations of dipolarization events in Mercury's magnetotail. J. Geophys. Res. 117, A00M03 (2012).

C. Tao, F. Sahraoui, D. Fontaine, J. de Patoul, T. Chust, S. Kasahara, A. Retinò, Properties of Jupiter's magnetospheric turbulence observed by the Galileo spacecraft. J. Geophys. Res. Space Physics. 120, 4 (2015).

J. G. Trotignon, C. Béghin, D. Lagoutte, J. L. Michau, H. Matsumoto, H. Kojima, K. Hashimoto, Y. Kasaba, L. G. Blomberg, J. P. Lebreton, A. Masson, M. Hamelin, R. Pottelette, Active measurement of the thermal electron density and temperature on the Mercury Magnetospheric Orbiter of the BepiColombo mission. Adv. Space Res. 38, (2006).

H. Tsunakawa et al., Lunar magnetic field observation and initial global mapping of lunar magnetic anomalies by MAP-LMAG onboard SELENE (Kaguya). Space Sci. Rev. 154, 1-4 (2010).

H. Yamakawa, H. Ogawa, Y. Sone, H. Hayakawa, Y. Kasaba, T. Takashima, T. Mukai, T. Tanaka, M. Adachi, Bepicolombo mercury magnetospheric orbiter design. Acta Astronautica, 62, (2008).

T. Yamamoto, A. Matsuoka, PLANET-B magnetic fields investigation. Earth Planets Space. 50, (1998).

S. D. Xiao, T. L. Zhang, Z. Vörös, Magnetic fluctuations and turbulence in the venusian magnetosheath downstream of different types of bow shock. J. Geophys. Res. Space Physics. 123, 10 (2018).

Figure 1: A magnetic energy spectrum measured by Messenger/MAG instruments in the Hermean magnetosheath (MS) close to the magnetopause. Three spectral bands with different power-law fits are evidenced. The vertical dashed line indicates the local ion gyrofrequency. Proton and Na+ gyrofrequencies are marked by black and green dashed lines, respectively. Adapted from Huang et al. (2020).

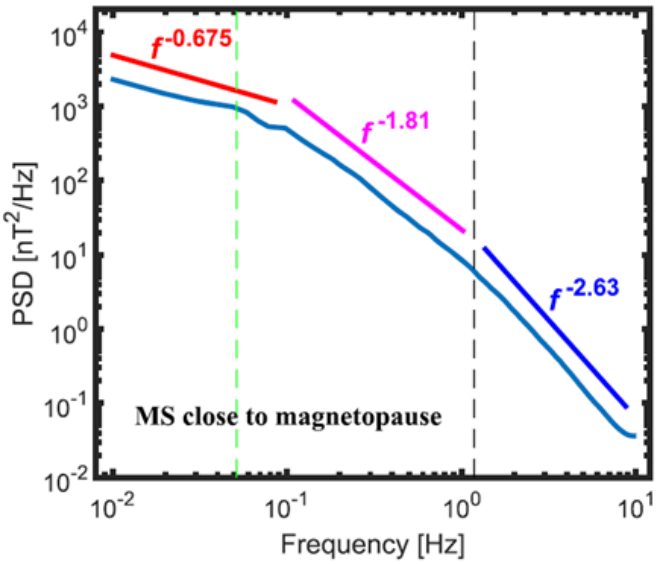

Figure 2: Example of the observations of whistler waves inside an electron vortex magnetic hole on 2015 November 3 by the MMS spacecraft in the magnetosheath. (a) Magnetic field strength; (b) the ratios between electron perpendicular temperature and parallel temperature; (c) filtered magnetic field fluctuations from the SCM instrument; (d)–(e) power spectral densities of the electric and magnetic components of the waves. The black, cyan, and red curves in (d)–(e) indicate the frequencies 0.1 f_{ce}, 0.5 f_{ce}, and 1.0 f_{ce}, respectively (f_{ce} is the electron gyrofrequency). Similar studies can be achieved in the Hermean environment using the LF-SC and DB-SC instruments onboard BepiColombo/MIO. Adapted from Huang et al. (2018).

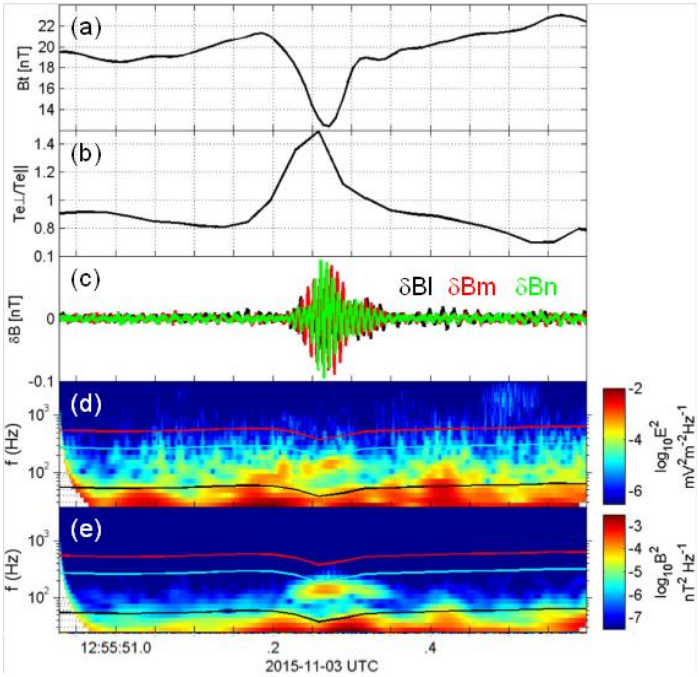

Figure 3: Configuration of electric and magnetic field sensors onboard the Mio spacecraft. The search coil sensors are placed on the tip of a 4.6-m mast extending from the spacecraft body. Another mast is deployed from the opposite side of the spacecraft for the DC magnetic field sensors (MGF) (Baumjohann et al., 2010; this issue).

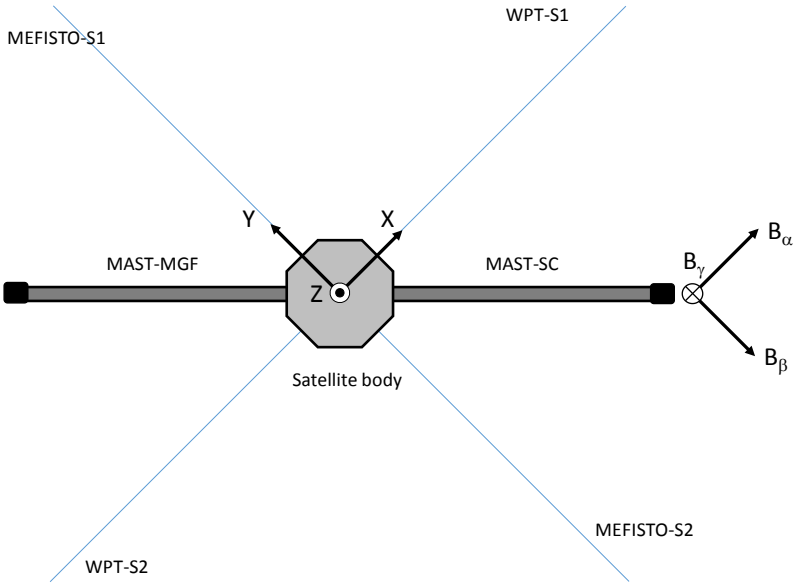

Figure 4: Configuration of the search coil sensors and the extendable mast. (a) An illustration of the sensors on top of a coilable mast extending from the canister. (b) The preamplifier box with the top panel opened. (c) The search coil sensors assembly on the mast top plate. (d) The fully extended mast system during a ground test, with the search coil sensors located at the mast's tip.

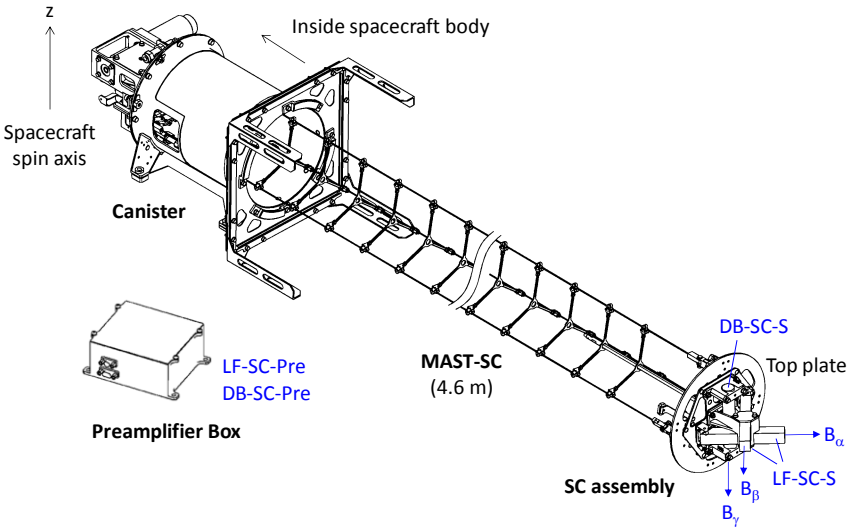

(a)

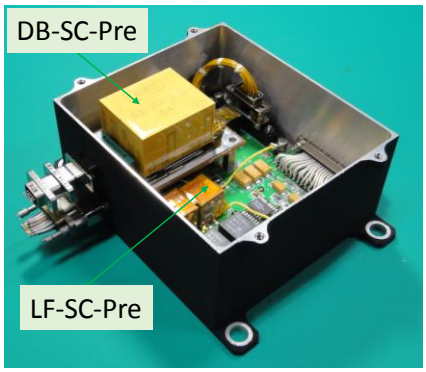

(b)

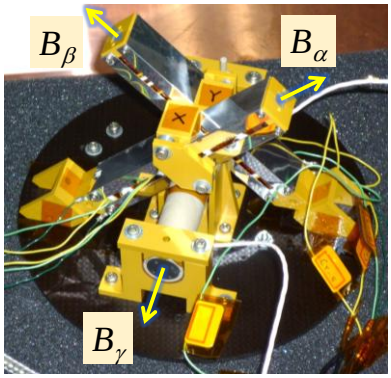

(c)

Figure 4 (continued)

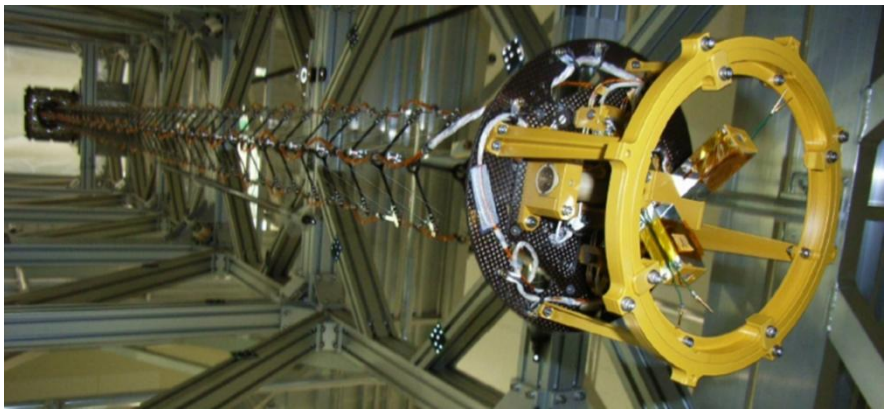

(d)

Figure 5: Block diagram of the search coil sensors and preamplifiers

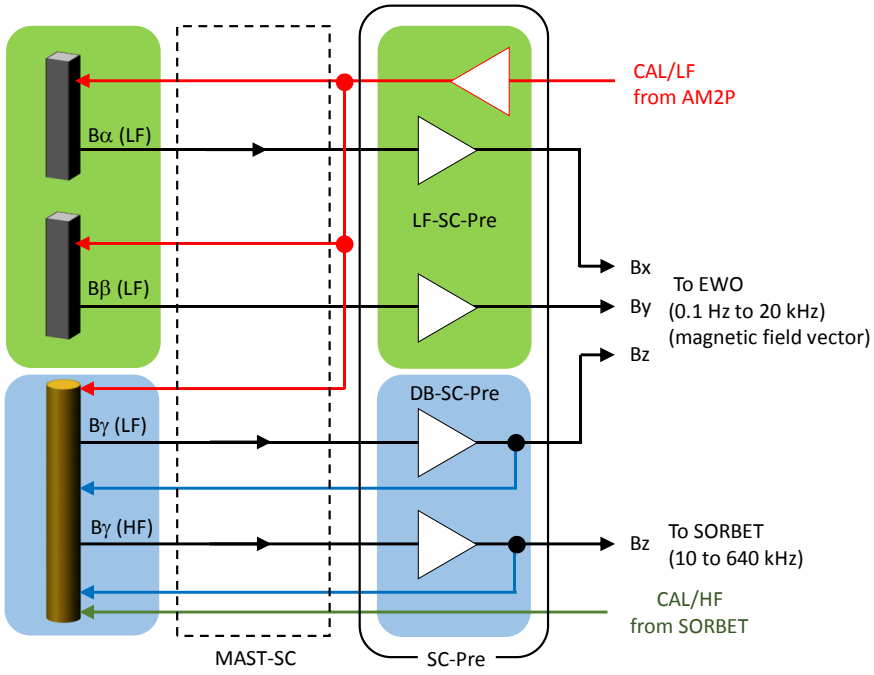

Figure 6: Sensitivities and dynamic ranges of search coil magnetometers combined with the EWO-WFC/OFA(B) and SORBET receivers. Also shown are the expected plasma and radio waves with spectral amplitudes corresponding to measurements in the terrestrial environment (Kasaba et al., this issue). The B_0 means the spin-modulated DC magnetic field to be measured around Mercury.

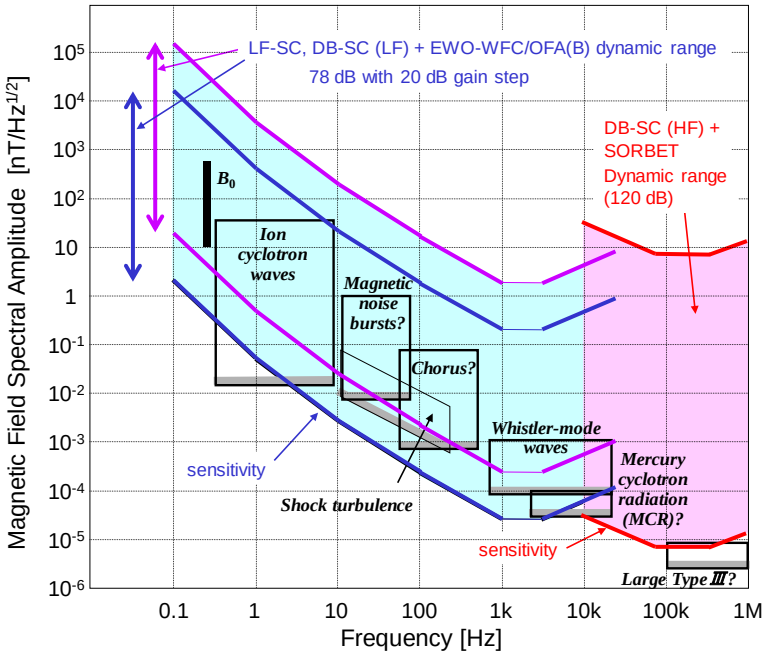

Figure 7: One axis sensor of LF-SC. (a) Structure and (b) the flight model of the one axis sensor.

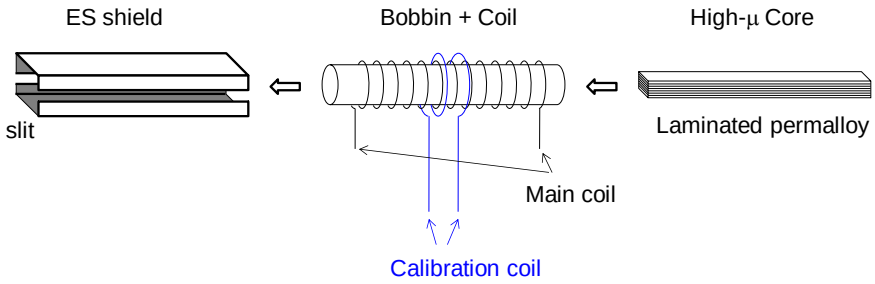

(a)

(b)

Figure 8: Equivalent circuit of the LF-SC sensor. For the meaning of the labels beside the circuit elements, refer to the text.

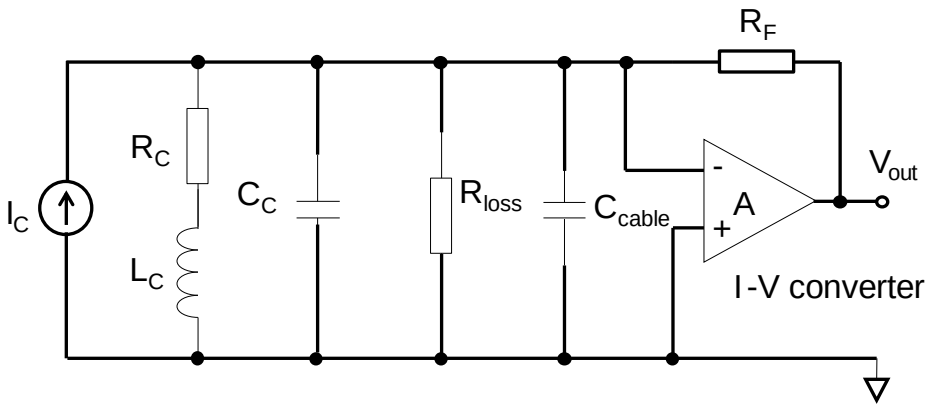

807 **Figure 9: Block diagram of the LF-SC sensors and preamplifiers.**

808

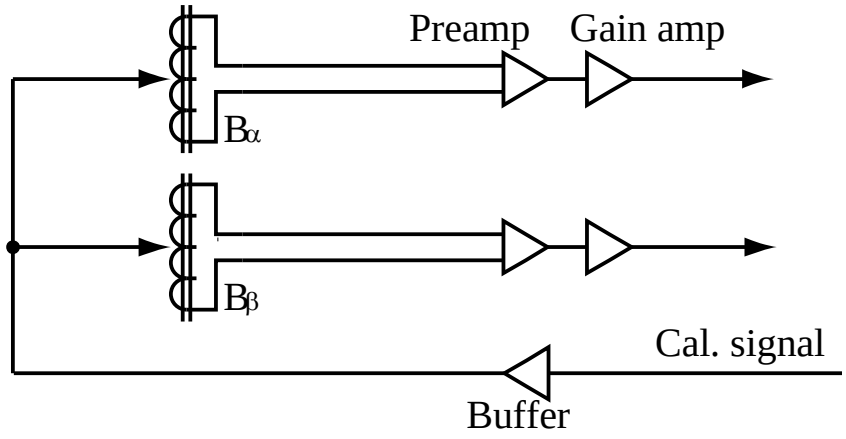

809

810

Figure 10: Structure of the DB-SC LF and HF sensors.

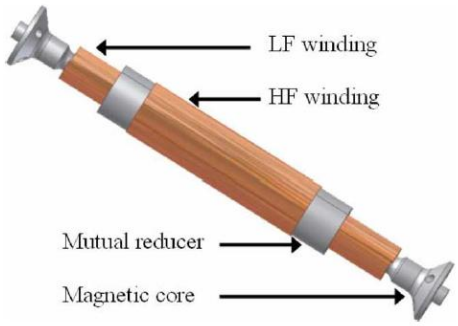

Figure 11: Gain, phase and sensitivity of the LF-SC measured on ground. Frequency characteristics of (a) gain, (b) phase and (c) noise floor (noise-equivalent magnetic induction: NEMI).

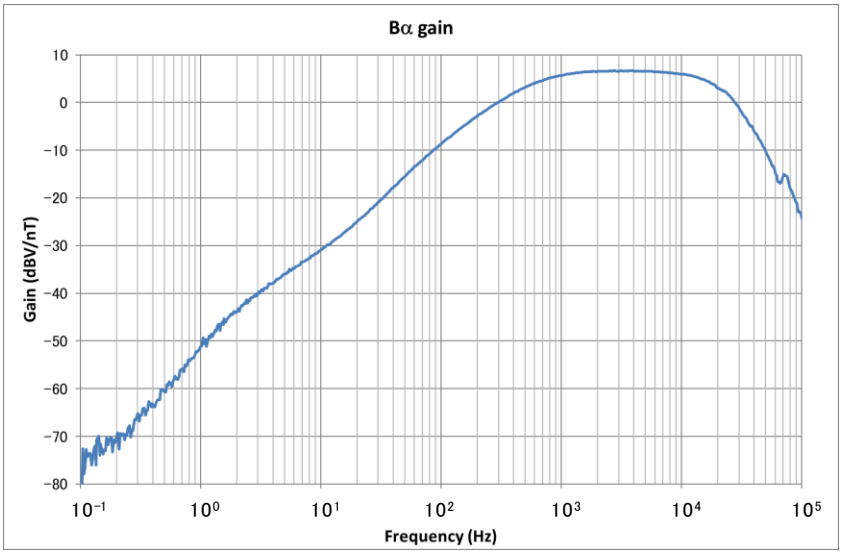

(a)

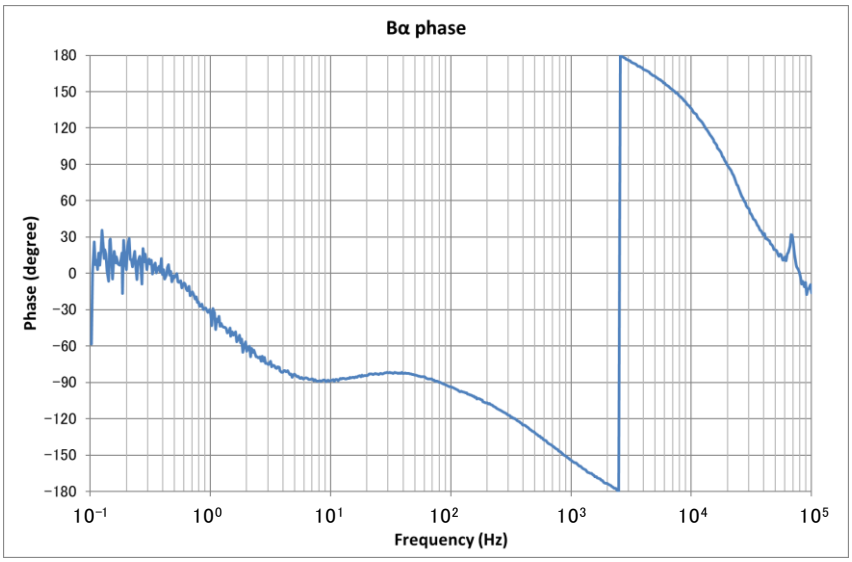

(b)

826 **Figure 11 (continued)**

827

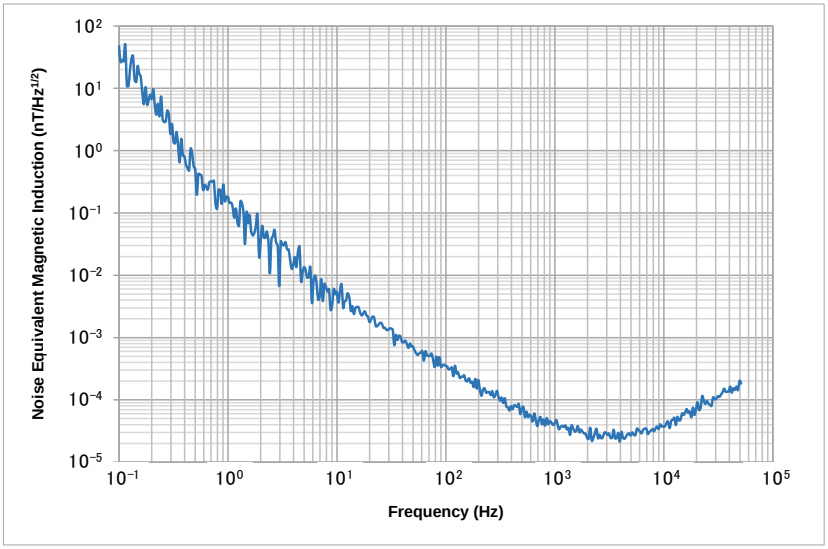

828

829 (c)

830

Figure 12: (a) Gain and (b) phase of DB-SC (LF) and (c) gain and (d) phase of DB-SC (HF) measured on the ground.

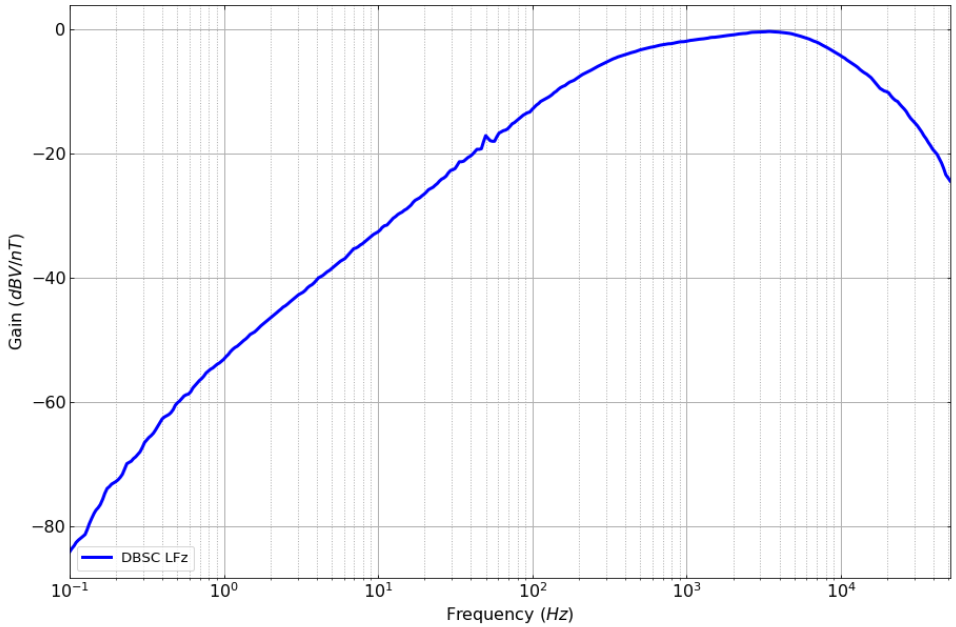

(a)

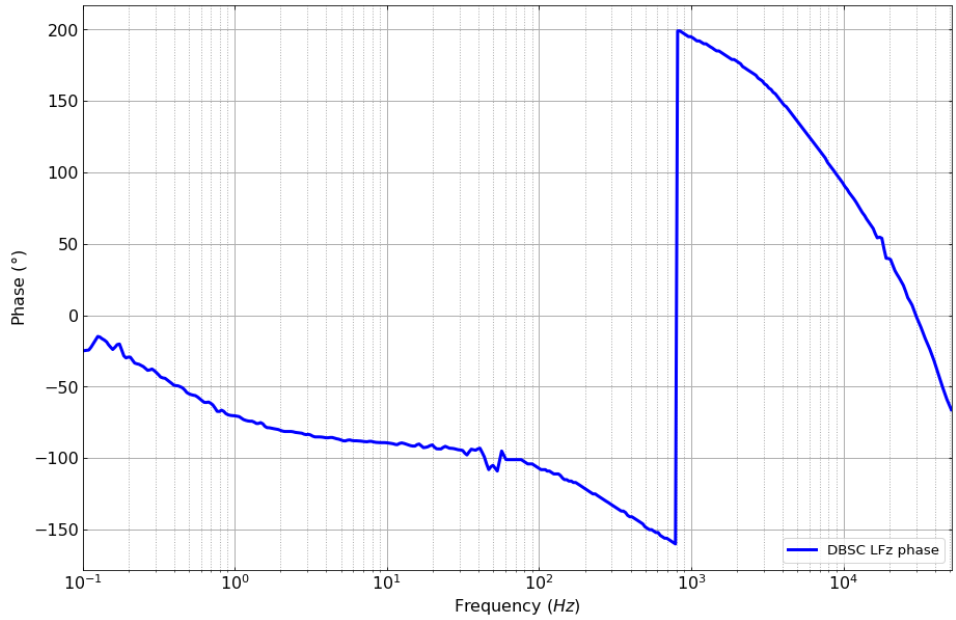

(b)

Figure 12: (continued)

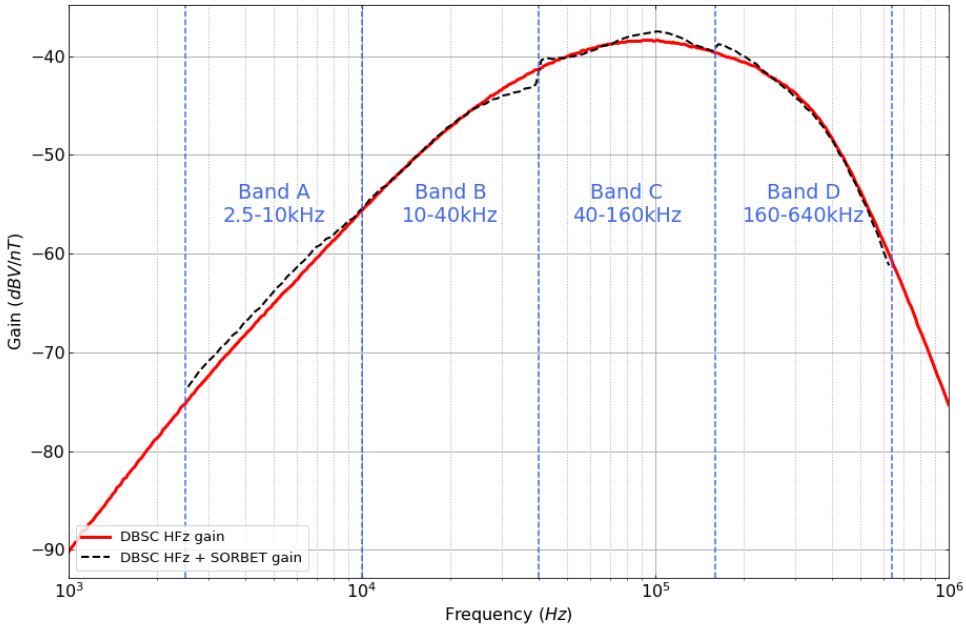

(c)

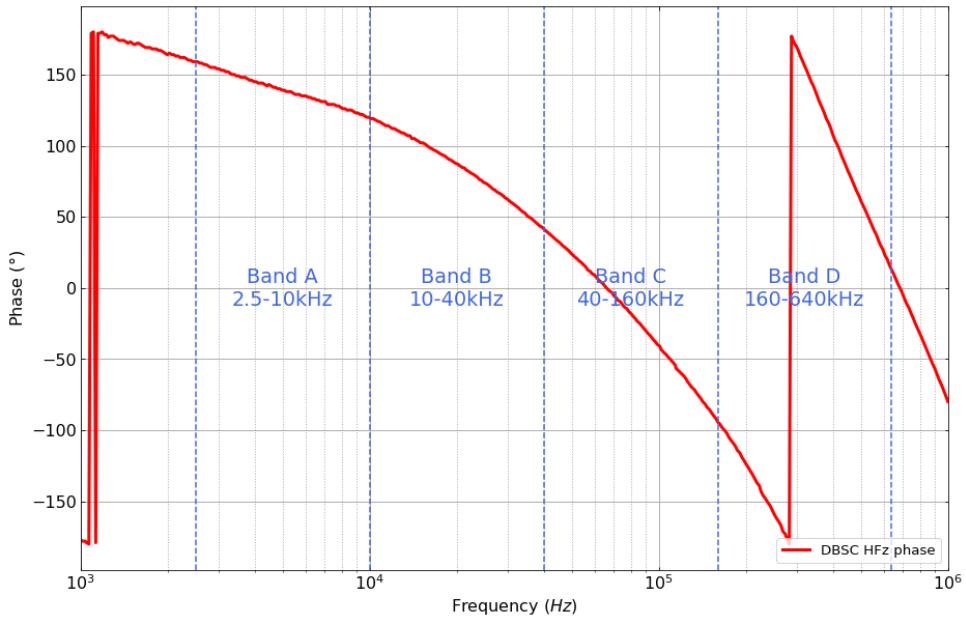

(d)

Figure 13: Noise floor (noise-equivalent magnetic induction: NEMI) of the DBSC (LF and HF) sensor and electronics measured on the ground.

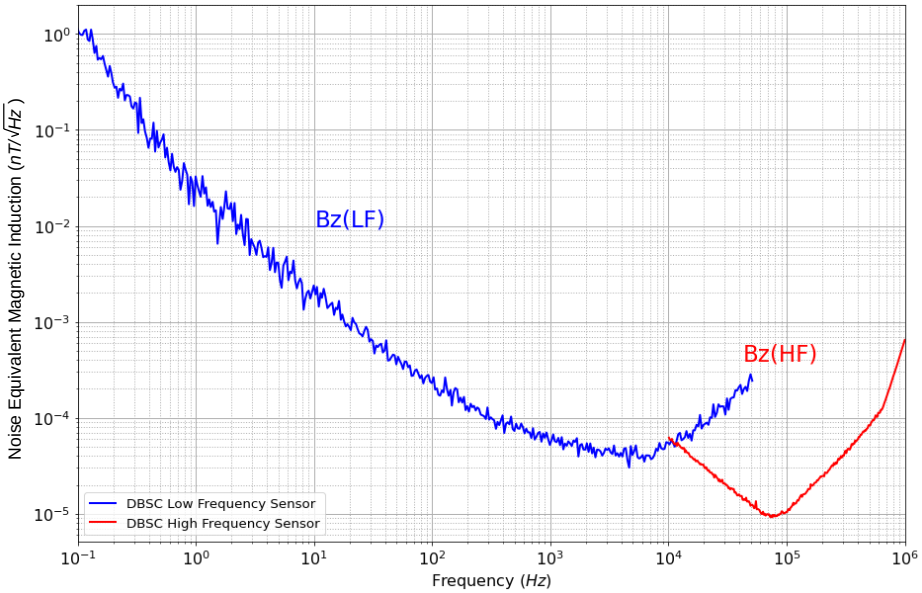

Figure 14: In-flight EWO data for low-frequency magnetic field during 01:00–02:00 UT on November 10, 2018, in the NECP campaign. (a) The dynamic spectra of $|B|$ converted using the noise gain for the three channels (see the text). (b) The frequency characteristics of magnetic field spectral amplitude: the red symbols show the profile averaged over the one hour in (a), while the black symbols plot the minimum value at each frequency bin observed in the same period. The blue curve is the noise spectrum of NEMI measured on the ground.

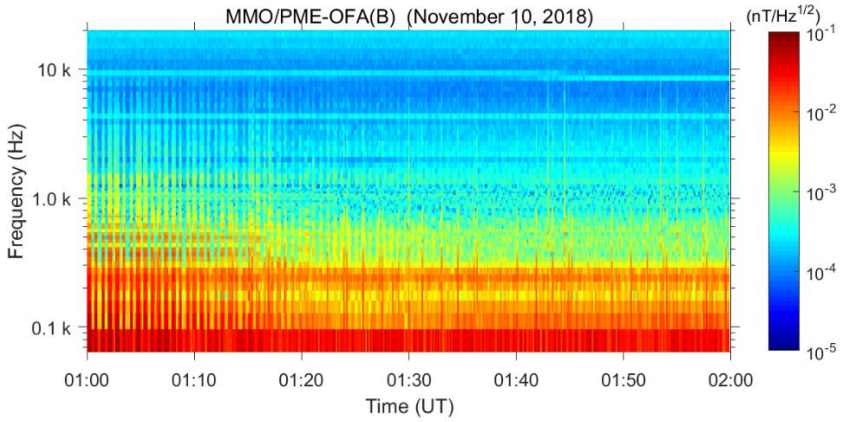

(a)

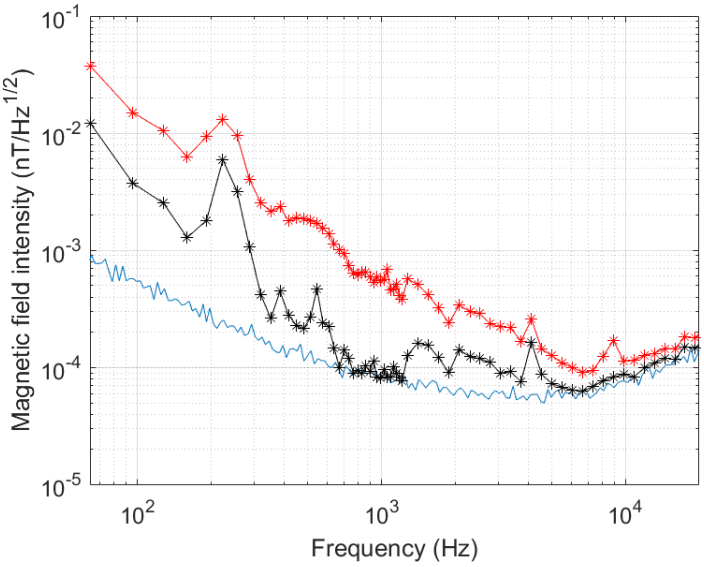

(b)

Figure 15: An in-flight calibration of the low-frequency sensors carried out on November 10, 2018 during NECP. The symbols represent the gain and phase of the transfer functions for the three sensors obtained by the onboard calibration. The blue lines show the profiles measured on ground.

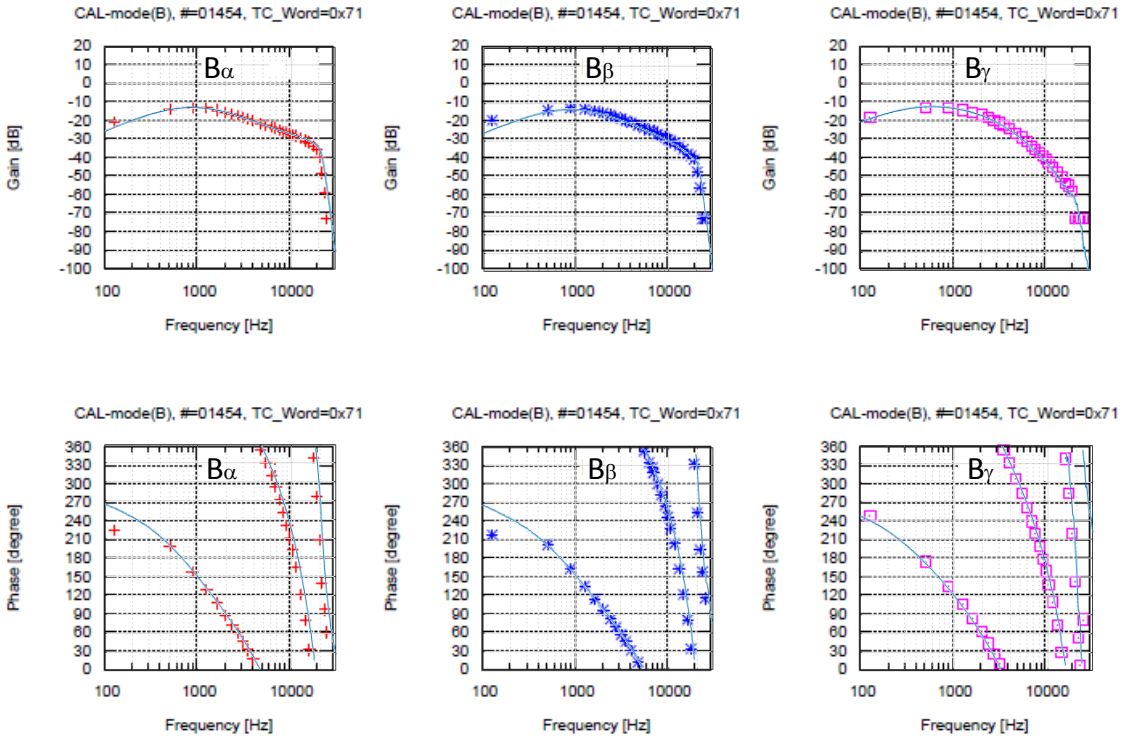

Figure 16: SORBET spectrogram of DB-SC (uncalibrated) data during NECP (the transfer function of DBSC is not included).

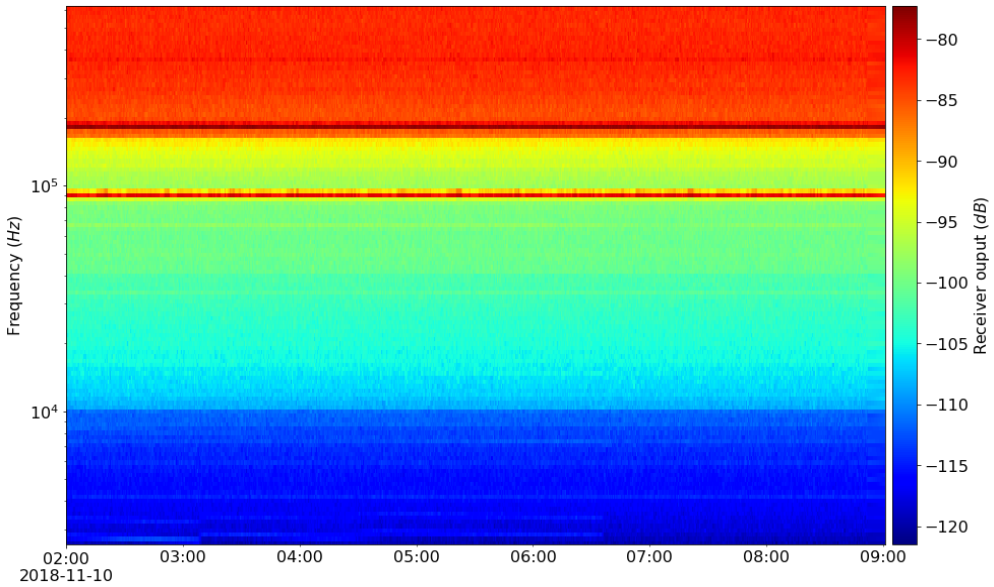

878 **Table 1: Summary of LF-SC and DB-SC specifications.**

879

880

881

Features	LF-SC	DB-SC
Sensors	194 grams (2 sensors) 14.4 × 17 ×116 mm	65 grams 17 mm (diameter) × 111 mm
Preamplifiers (in total)	324.7 grams, 100 × 90 × 48.2 mm	
Power (in total)	+/-12V, 384 mW	
Performance	0.1 Hz – 20 kHz	0.1 Hz – 20 kHz (LF) 10 kHz – 640 kHz (HF)
Sensitivity at 10 Hz pT/Hz$^{1/2}$	3	2 (LF)
Sensitivity at 1 kHz fT/Hz$^{1/2}$	40	50 (LF)
Sensitivity at 10 kHz fT/Hz$^{1/2}$	40	50 (HF)
Sensitivity at 100 kHz fT/Hz$^{1/2}$		10 (HF)

882

883